Solar Energy Materials & Solar Cells 157 (2016) 660–665

Contents lists available at ScienceDirect

Solar Energy Materials & Solar Cells

journal homepage: www.elsevier.com/locate/solmat

# Flexible and efficient ITO-free semitransparent perovskite solar cells

Xia-Li Ou [a], Ming Xu [a], Jing Feng [a,*], Hong-Bo Sun [a,b]

[a] State Key Laboratory on Integrated Optoelectronics, College of Electronic Science and Engineering, Jilin University, 2699 Qianjin Street, Changchun 130012, People's Republic of China

[b] College of Physics, Jilin University, 119 Jiefang Road, Changchun 130023, People's Republic of China

ARTICLE INFO

*Article history:*
Received 2 June 2016
Received in revised form
7 July 2016
Accepted 11 July 2016

*Keywords:*
Perovskite solar cells
Semitransparent
Flexible
ITO-free

ABSTRACT

Semitransparent perovskite solar cells (PeSCs) with high efficiency and flexibility are demonstrated by using ultrathin Au and dielectric/metal/dielectric multilayered films as bottom and top electrode, respectively. An overall power conversion efficiency (PCE) of 8.67% and an average light transmittance (ALT) of 15.94% in the wavelength range of 500–2000 nm were obtained for the PeSCs. The ALT can be further increased to 31.61% by reducing the thickness of the bottom Au electrode. Furthermore, the PeSCs show excellent flexibility and mechanical robustness, and the PCE maintains 88% of their original efficiencies after 1000 bending cycles with a bending radius of 3.9 mm.



## 1. Introduction

Recently, flexible and semitransparent solar cells have been extensively investigated for their potential in some special applications such as wearable electronics and building-integrated photovoltaics [1–4]. Organic solar cells have merits of light-weight, portability and compatibility with wearable forms, however, low photovoltaic performance and stability have been huge obstacles in their development [5–8]. Meanwhile, the lab-scale power conversion efficiency (PCE) of the solar cell based on hybrid organic-inorganic halide perovskite (e.g., $CH_3NH_3PbX_3$, X=Cl, Br, I) has skyrocketed from 3.8% to the latest higher than 20% since their first reported in 2009 [9–13]. In additional to high efficiency, perovskite solar cells (PeSCs) are mechanically flexible, low-temperature solution-processible and exploit low cost [14–16]. Hence, PeSCs have emerged at the forefront of such kind of flexible and semitransparent photovoltaic research. Indium tin oxide (ITO) sputtered on plastic substrates has been mostly used as standard transparent electrode in flexible PeSCs. Despite the high PCE with slight flexibility have been reported, the use of brittle ITO limited the design of highly deformable device architectures, because ITO is likely to generate cracks under repeated bending [17–20]. Hence, flexible PeSCs based on high conductivity and bendable electrodes such as thin graphene [21,22], carbon nanotubes [23], silver nanowires [24,25] and conductive polymers [14,26] have already been designed. Most of them result in poor performance except the PeSCs based on graphene. Nevertheless, transfer and lamination procedures involved in the preparation of graphene have increased the complexity of the device fabrication. Hence, although the PCE of PeSCs have been greatly improved through optimizing the structure of PeSCs as optimization show great importance on improving the performance of devices [27–32], a simple and low-cost electrode with high transparency and conductivity for the flexible and semitransparent PeSCs is still a challenge.

In this work, thin Au bottom electrode and dielectric/metal/dielectric (DMD) multilayered top electrode have been employed to obtain flexible and efficient ITO-free semitransparent PeSCs. Herein, the thin Au layer is selected for its simple preparation process, considerable mechanical robustness and flexibility. The DMD transparent electrode with structure of bottom molybdenum trioxide (b-$MoO_3$)/Au/Ag/top $MoO_3$ (t-$MoO_3$)/Tris-8-hydroxyquinoline aluminum ($Alq_3$) stack exhibits high transparency, conductivity and flexibility. These semitransparent PeSCs exhibit considerable PCE of 8.67% which is among the highest PCEs of so far reported semitransparent single-junction PeSCs to the best of our knowledge [1,33–35]. Furthermore, these PeSCs shown excellent flexibility as 88% of their original efficiencies were maintained after 1000 bending cycles with a bending radius (r) of 3.9 mm which is also much better than reported flexible PeSCs based on ITO electrode which show slight flexibility (r=7–10 mm) [17–20].

## 2. Experimental details

### 2.1. Materials

All chemicals have been used as received without any further purification. $CH_3NH_3I$ (MAI, 99.5%) has been purchased from Xi'an

* Corresponding author.
*E-mail address:* jingfeng@jlu.edu.cn (J. Feng).

http://dx.doi.org/10.1016/j.solmat.2016.07.010
0927-0248/

Polymer Light Technology Corp. Poly (3, 4-ethylenedioxythiophene): poly (styrenesulfonate) (PEDOT: PSS) (Al4083), lead chloride ($PbCl_2$, 99.99%), [6, 6]-phenyl C61-butyric acid methyl ester (PCBM) and $MoO_3$ (99.5%) have been purchased from Luminescence Technology Corp. $Alq_3$ (99.5%) has been purchased from Jilin OLED Material Tech co., Ltd.

### 2.2. Fabrication of the PeSCs

In the device architecture, low-temperature processable PEDOT:PSS and PCBM are used as hole transport and electron transport layers, respectively. The PeSCs with the architecture of Au/PEDOT: PSS/$CH_3NH_3PbI_3$-xClx/PCBM/DMD top electrode have been fabricated by the following processes. Firstly, flexible substrate was prepared by spin coating the photopolymer (NOA63, Noland Optical Adhesive 63) at 7000 revolutions per minute (rpm) for 30 s on a pre-hydrophobic treated Si wafer and then the photopolymer was cured by UV-ozone ($UV/O_3$) treatment. The NOA63 was peeled-off from the Si wafer, after that Au films with various thicknesses were thermal deposited onto the NOA63 substrate as bottom electrode at a rate of 0. 9 Å/s and a base pressure of $5 \times 10^{-4}$ Pa and treated with $UV/O_3$ for 5 min. PEDOT: PSS (~55 nm) was deposited onto the surface of Au electrode as hole transport layer by spin coating at 3500 rpm for 1 min and annealing at 95 °C for 20 min in nitrogen atmosphere in sequence. Perovskite absorber layer was prepared as follows. A 1:3 M ratio of mixed $PbCl_2/CH_3NH_3I$ perovskite precursor solution was spin coated onto the PEDOT: PSS layer, and during the spinning process, toluene (80 μL) was dripped onto the center of the spinning substrate with a delay time of 25 s to remove excess solvent that did not coordinate with $PbCl_2$/MAI [36,37]. In order to enhance the ALT of the PeSCs, perovskite layer was fabricated with a rotation speed of 6000 rpm to obtain a thickness of 240 nm [33,38]. The uniform and transparent perovskite film was formed by annealing at 95 °C for 70 min in dimethylformamide (DMF) vapor atmospheres and then annealing for another 20 min after removing the vapor atmospheres. Afterwards, 2 wt% PCBM in chlorobenzene solution was spin coated as electron transport layer (~55 nm) at 1500 rpm and then annealing at room temperature overnight. Finally, the solar cells were completed by thermal evaporating DMD electrodes composed of: (i) a b-$MoO_3$ layer (2 nm); (ii) a thin Au film (1 nm); (iii) a thin Ag film (7 nm); (IV) a t-$MoO_3$ layer (5 nm); and (V) a $Alq_3$ film (50 nm) under vacuum of $5 \times 10^{-4}$. The deposition rates were set to be 1 Å/s for all layers, and the thicknesses were monitored by quartz crystals. The PeSCs based on the ITO bottom electrode and the DMD top electrode are fabricated for comparison.

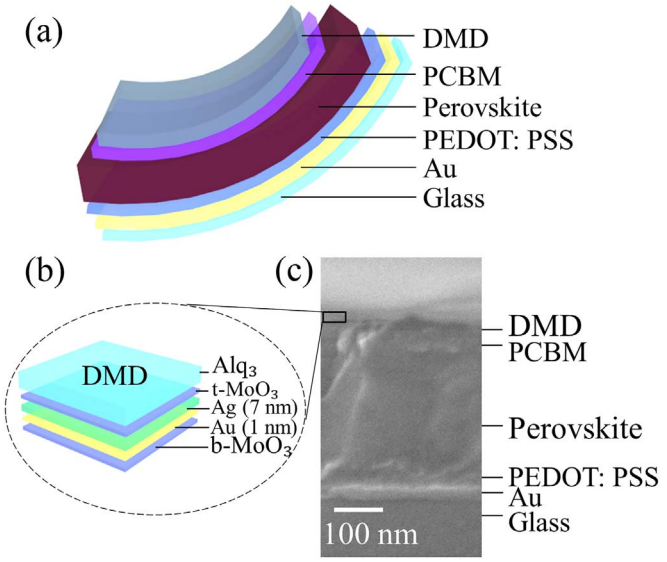


**Fig. 1.** (a) Structure of the semitransparent flexible PeSCs. (b) Structure of the DMD multilayered top electrode. (c) SEM cross-sectional image of the PeSCs.

## 3. Results and discussion

The schematic illustration of the solution-processed PeSCs and the DMD electrode are shown in Fig. 1(a) and (b), respectively. In this study, Noland NOA63 photopolymer with a transmittance of

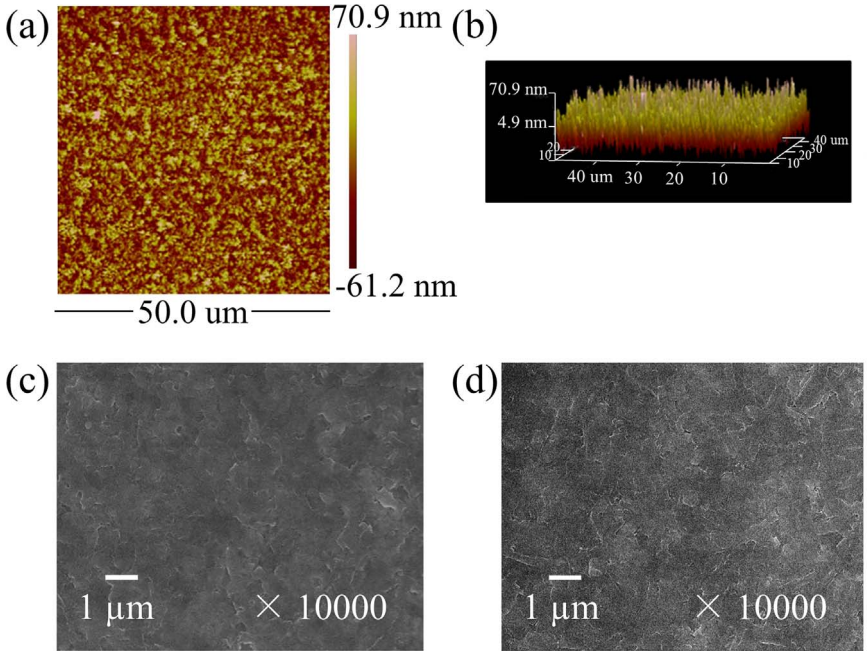


**Fig. 2.** AFM and SEM images of perovskite films fabricated by one step method using $CH_3NH_3PbI_{3-x}Cl_x$ precursor. (a) 2D and (b) 3D AFM images of perovskite film deposited on PEDOT:PSS/Au/NOA63 substrate in the area of 50 μm × 50 μm. Top-view SEM images of perovskite films deposited on PEDOT:PSS/ITO (c) and PEDOT:PSS/Au/NOA63 (d) substrates.

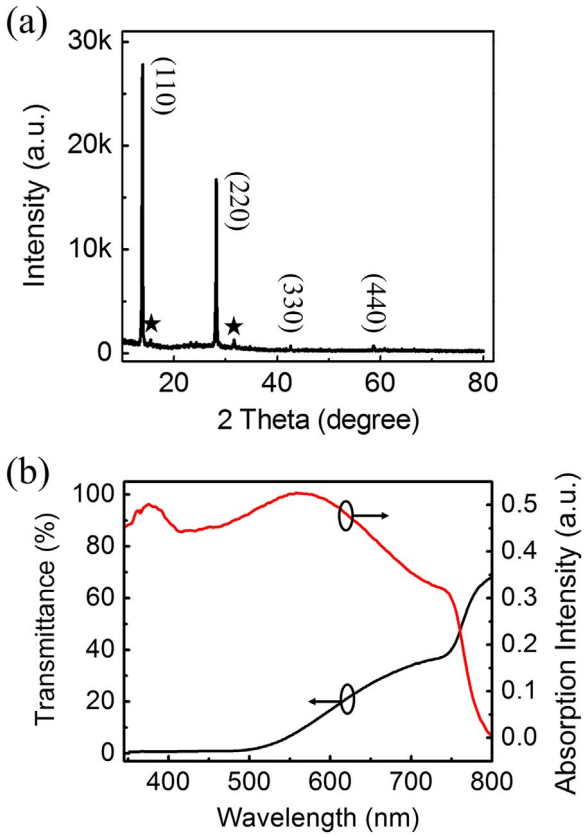


**Fig. 3.** Characteristics of $CH_3NH_3PbI_{3-x}Cl_x$ perovskite films on PEDOT:PSS/NOA63 substrate. (a) XRD patterns. (b) UV-vis absorbance and transmittance spectra.

91% in the whole visible wavelength range is selected as substrate. As it can be seen in the cross-sectional scanning electron microscopic (SEM), there is little-to-no observable interdiffusion between layers (Fig. 1(c)). The morphology of the perovskite thin film is evaluated by atomic force microscopy (AFM) and top-view SEM. As can be estimated from AFM images (Fig. 2(a) and (b)) in the area of 50 μm × 50 μm, the root-mean-square surface roughness (RMS) of perovskite film is 20.6 nm, which is as small as the roughness of the film fabricated via other methods [39–41]. Meanwhile the SEM images of perovskite films on PEDOT:PSS/ITO and PEDOT:PSS/Au/NOA63 substrate are shown in Fig. 2(c) and (d), respectively, which exhibit no obvious difference and both films show large grain size up to micrometer scale without pinholes.

To further study the crystallinity of perovskite films, X-ray diffraction (XRD) pattern was analyzed and shown in Fig. 3(a). The patterns were accumulated by an X-ray diffractometer (Shimadzu XRD-6000) with a monochromated high-intensity Cu Kα radiation of wavelength of 0.15418 nm operated at 40 kV and 20 mA on perovskite films. The divergence and scattering slits were set at 2/3°, and the receiving slit was set at 0.3 mm. XRD of 5 perovskite films was measured and shown similar intensities of the characteristic diffraction peaks. The peaks located at 13.88°, 28.22°, 42.62°, and 58.72° are assigned to (110), (220), (330), and (440) planes of tetragonal $CH_3NH_3PbI_{3-x}Cl_x$, respectively [42–44]. The peaks marked with stars which located at 15.46° and 31.66° are assigned to cubic phase trichloride perovskite, $CH_3NH_3PbCl_3$ [45]. The absence of intense and characteristic XRD peak of $PbCl_2$ at 22.68° indicate the complete conversion of $PbCl_2$ and the strong peaks of (110) and (220) manifest the dominant in-plane growth of perovskite grains. The typical absorption and corresponding transmittance spectrum of the thin perovskite film were shown in Fig. 3(b), and the highest transmittance is found to be about 75% at 800 nm.

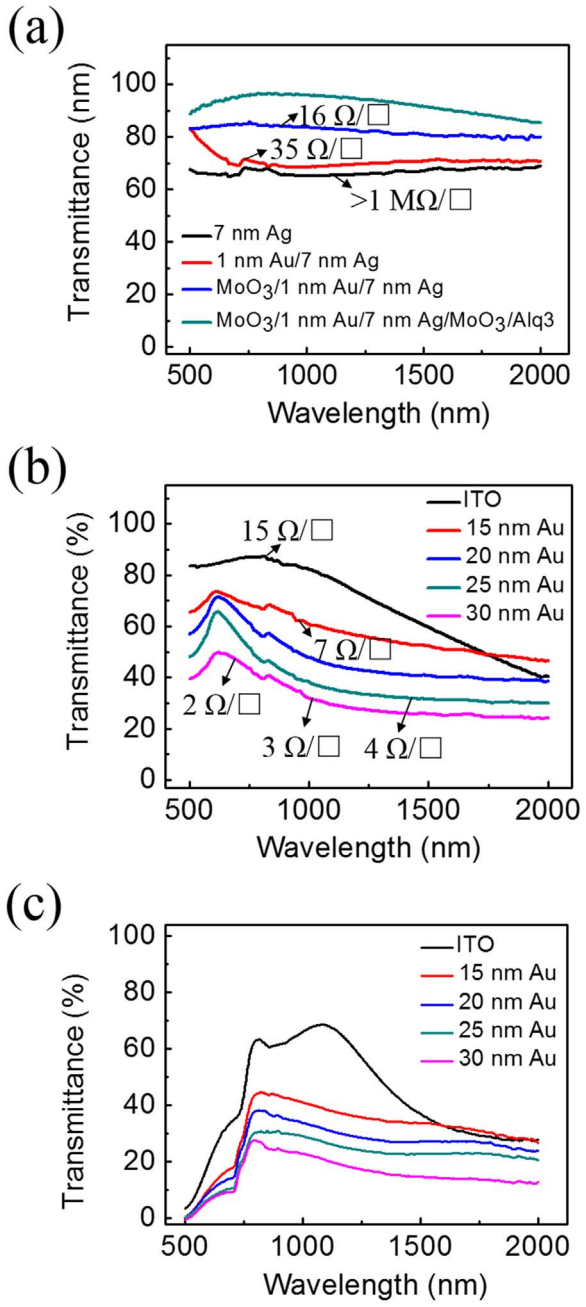


**Fig. 4.** Transmittances of electrodes and whole device. (a) Transmittance and $R_S$ of 7 nm Ag layers (black), 1 nm Au/7 nm Ag (red), b-$MoO_3$/1 nm Au/7 nm Ag (blue) and b-$MoO_3$/1 nm Au/7 nm Ag/t-$MoO_3$/$Alq_3$ (green). (b) Transmittances and $R_S$ of ITO and Au layers with various thicknesses which have been annealed for 110 min at 95 °C. (c) Transmittances of whole devices based on DMD top electrode and various bottom electrodes. (For interpretation of the references to color in this figure legend, the reader is referred to the web version of this article.)

Transparent electrode is one of the key components for the semitransparent PeSCs. Hence, the transmittance spectra and corresponding sheet resistances ($R_S$) of the top DMD and bottom Au electrodes with various layer structures and parameters, and the whole PeSCs are investigated. In the DMD architecture, a ultrathin Au layer was chosen as a seed layer to modulate the surface energy and optimize the growth conditions for silver [46], two $MoO_3$ layers were acted as dielectric to increase the transparency of electrode [47], and an organic capping of $Alq_3$ film was served to enhance light incoupling [48,49]. As shown in Fig. 4(a), the DMD

multilayered electrode with b-$MoO_3$/Au/Ag/t-$MoO_3$/$Alq_3$ architecture features an ALT of 88.67% at the wavelength range of 500–2000 nm, which is much enhanced when compared to that of the Ag single layer, Au/Ag double layer and b-$MoO_3$/Au/Ag, and even conventional transparent ITO (ALT=68.40% as shown in Fig. 4(b)). Moreover, the sheet resistance (Rs) of 7 nm silver film is reduced by several orders of magnitude from $>1M\Omega/\square$ to around $35\ \Omega/\square$ (1 nm Au/7 nm Ag) by introducing a ultrathin Au layer as a seed layer. The Rs is further reduced from $35\ \Omega/\square$ to $16\ \Omega/\square$ (b-$MoO_3$/Au/Ag/t-$MoO_3$/$Alq_3$) by introducing a b-$MoO_3$. Fig. 4(b) shows the comparisons of transmittance spectra and Rs of ITO and different thicknesses Au layers which were annealed at 95 °C for 110 min. As it can be seen in spectra of different thicknesses Au layers (Fig. 4 (b)), there exist a peak at about 600 nm and transmittances decrease with the increase of the wavelength from 600 nm to1000 nm and then maintain stable in the wavelength range of 1000–2000 nm. The ALT of ITO and 15 nm, 20 nm, 25 nm, 30 nm Au films are about 69.51%, 59.92%, 45.43%, 38.69, 32.54%, respectively. Here,

**Table 1**
The average photovoltaic parameters of 12 PeSCs based on different bottom electrodes illuminated from both top and bottom sides.

| Electrode | Illumination side | Voc (V) | Jsc (mA/cm$^2$) | FF (%) | PCE (%) | ALT (%) |
|---|---|---|---|---|---|---|
| **ITO** | Top | 0.943 | 18.21 | 70.02 | 12.02 | 42.65 |
| | Bottom | 0.941 | 18.13 | 68.21 | 11.64 | |
| **30 nm Au** | Top | 0.940 | 14.67 | 62.34 | 8.60 | 15.94 |
| | Bottom | 0.838 | 8.09 | 53.48 | 3.63 | |
| **25 nm Au** | Top | 0.937 | 13.86 | 62.01 | 8.05 | 22.08 |
| | Bottom | 0.849 | 9.34 | 48.83 | 3.87 | |
| **20 nm Au** | Top | 0.847 | 12.78 | 59.62 | 6.45 | 26.28 |
| | Bottom | 0.818 | 10.26 | 47.02 | 3.95 | |
| **15 nm Au** | Top | 0.790 | 9.25 | 54.91 | 4.01 | 31.61 |
| | Bottom | 0.719 | 8.11 | 58.80 | 3.43 | |

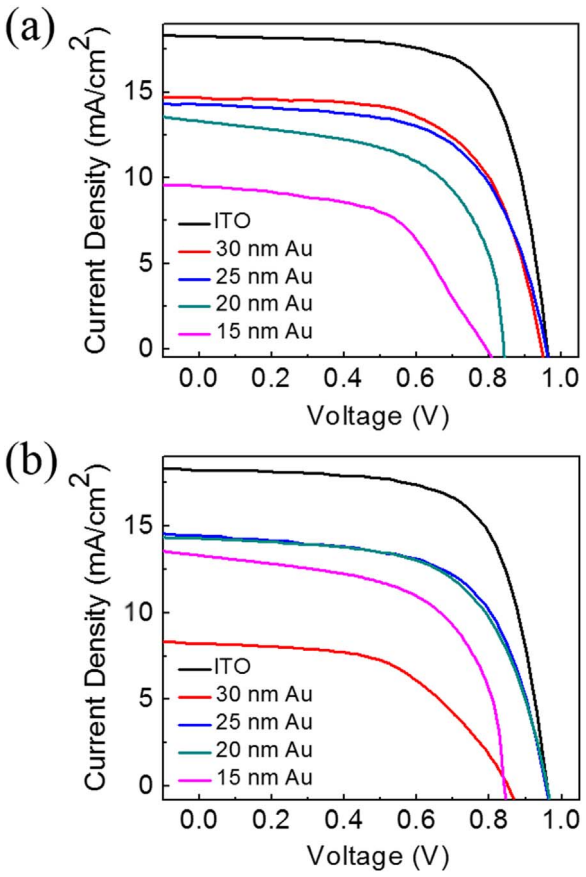


**Fig. 6.** J-V curves of the best performance PeSCs based on various bottom electrodes illuminated from top (a) and bottom (b) side.

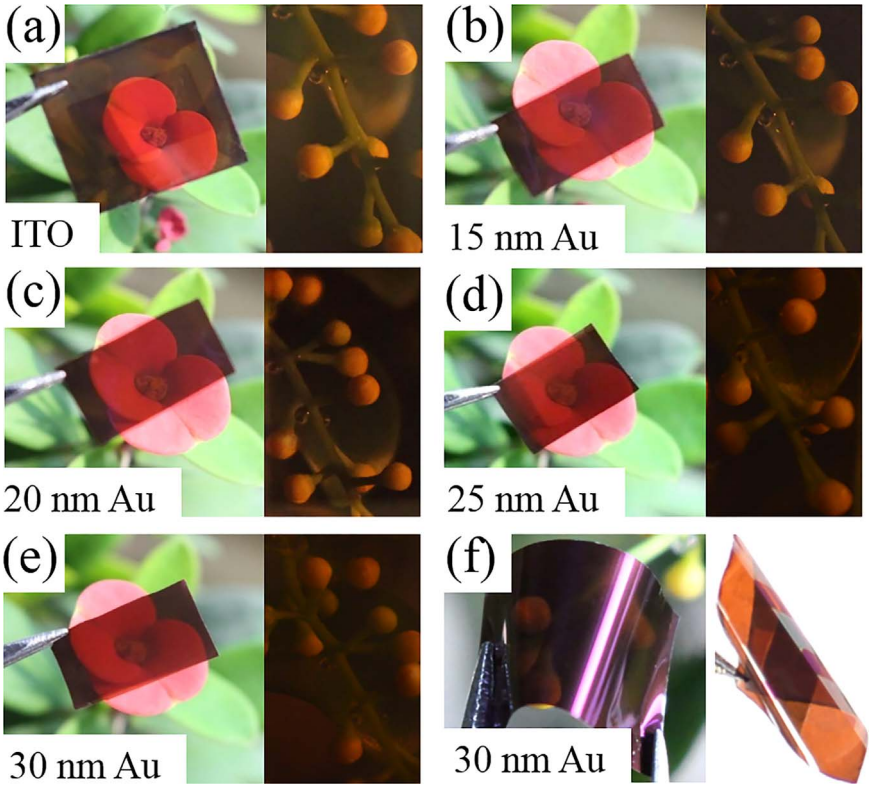


**Fig. 5.** Photographs of flexible and semitransparent PeSCs based on DMD top electrode and different bottom electrodes: (a) ITO, (b) 15 nm Au, (c) 20 nm Au, (d) 25 nm Au and (e) 30 nm Au. (f) Photographs showing the bending PeSCs.

the flexibility of transparency and efficiency of devices was managed by simply controlling the thickness of the bottom Au electrodes. The transmittance spectra and the precise ALT values of the whole devices based on DMD top electrode and various thicknesses Au bottom electrodes were illustrated in Fig. 4(c) and Table 1, respectively. As it can be figured out, the transmittances of devices in the wavelength range of 500–800 nm and 800–2000 nm are mainly depend on the transmittances of perovskite film and Au bottom electrodes, respectively. The semitransparent PeSCs achieve an ALT of 42.65% by utilizing ITO as bottom electrode. Then, after replacing the expensive and fragile ITO to a robust and flexible 30 nm Au electrode, an ALT of 15.94% were obtained. Meanwhile, in order to improve the ALT, the thickness of Au electrode was reduced to 25 nm, 20 nm and 15 nm, and the corresponding ALT of 22.08%, 26.28% and 31.61% were obtained, respectively. Besides, the corresponding photographs of the PeSCs taken in front of red and yellow flowers are shown in Fig. 5(a–e) as corroborative evidences of the high device ALT.

Fig. 6 illustrates the best performance of the PeSCs based on DMD top electrode and different thicknesses Au bottom electrodes investigated under simulated AM 1.5G with a light intensity of 100 mW $cm^{-2}$ illuminated from both top and bottom sides. The average photovoltaic parameters of PeSCs typically derived from 12 devices are summarized in Table 1. The PeSCs based on ITO bottom electrode show an ALT value of 42.65%, the best PCEs of 12.13% and 11.91%, average PCEs of 12 devices of 12.02% and 11.64%, for top and bottom illumination, respectively. When using 30 nm robust and flexible Au as bottom electrode, an ALT of 15.94% with the best overall PCE of 8.67%' and 3.73%, average PCEs of 12 devices of 8.60% and 3.63% were obtained for top and bottom illumination, respectively. Through optimizing electrodes, the transparency and efficiency of devices were balanced and turn out enhanced ALTs of 22.08% (the best PCE=8.17%), 26.28% (the best PCE=6.71%) and 31.61% (the best PCE=4.11%) when thinner gold electrode of 25, 20 and 15 nm were used in PeSCs, respectively.

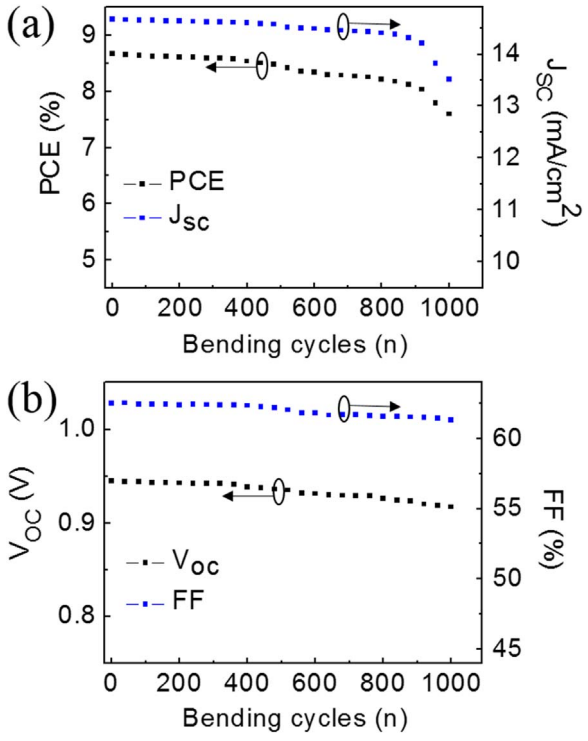


**Fig. 7.** Device performance for PeSCs as a function of bending cycles: (a) PCE and Jsc and (b) Voc and FF.

Hence, the best PCE of 8.67% and the highest ALT of 31.61% were achieved in these ITO-free PeSCs.

In order to determine the mechanical robustness of the PeSCs devices, a bending test was carried out and the photographs of the bending device were given in Fig. 5(f). The variations of the device performance with increasing bending cycles were traced. As shown in Fig. 7, after 1000 bending cycles with a bending radius of 3.9 mm, PeSCs based on 30 nm Au electrode exhibited slight decrease in PCE, retaining 88% of their original efficiencies without obvious deterioration of the key photovoltaic properties such as Jsc, Voc, and filling factor. Considering the high yield strength and elastic modulus of the perovskite film and the robustness and bendability of other components such as PEDOT:PSS and PCBM in these devices [14,50], the degradation of PCE should be ascribed to the small cracks occurs in electrodes which resulted in increasing resistance, and this degradation is much smaller than past reported flexible PeSCs based on ITO electrode [3,51,52].

## 4. Conclusions

In summary, flexible and efficient ITO-free semitransparent PeSCs have been demonstrated by utilizing a mechanically robust and flexible Au thin film and a highly conductive and transparent DMD multilayered film as bottom and top electrode, respectively. A PCE of 8.67% and an ALT of 15.94% in the wavelength range of 500–2000 nm were obtained for the PeSCs based on 30 nm Au bottom electrode. The PeSCs shows excellent mechanical robustness as it maintained 88% of its original PCE after 1000 bending cycles with a bending radius of 3.9 mm. These PeSCs suggest their compatibility for scale-up fabrication, which paves the way for commercialization of perovskite photovoltaic technology. The high efficiency and transparency, and as well as mechanical robustness indicate the potential of the ITO-free PeSCs in the building-integrated photovoltaics and wearable electronics.

## Acknowledgment

The authors gratefully acknowledge support from the 973 Project (2013CBA01700) and NSFC (Grant nos. 61322402, 91233123 and 61177024).

## References

[1] G.E. Eperon, D. Bryant, J. Troughton, S.D. Stranks, M.B. Johnston, T. Watson, D. A. Worsley, H.J. Snaith, Efficient, semitransparent neutral-colored solar cells based on microstructured formamidinium lead trihalide perovskite, J. Phys. Chem. Lett. 6 (2014) 129–138.
[2] C. Roldán-Carmona, O. Malinkiewicz, R. Betancur, G. Longo, C. Momblona, F. Jaramillo, L. Camacho, H.J. Bolink, High efficiency single-junction semitransparent perovskite solar cells, Energy Environ. Sci. 7 (2014) 2968.
[3] B.J. Kim, D.H. Kim, Y.-Y. Lee, H.-W. Shin, G.S. Han, J.S. Hong, K. Mahmood, T. K. Ahn, Y.-C. Joo, K.S. Hong, N.-G. Park, S. Lee, H.S. Jung, Highly efficient and bending durable perovskite solar cells: toward a wearable power source, Energy Environ. Sci. 8 (2015) 916–921.
[4] S.H. Lee, S.J. Yun, M. Shin, J.W. Lim, $Cu_2O$ thin films as the color-adjusting layer in semi-transparent a-Si:H solar cells, Sol. Energy Mater. Sol. Cells 117 (2013) 519–525.
[5] T.F. O'Connor, A.V. Zaretski, S. Savagatrup, A.D. Printz, C.D. Wilkes, M.I. Diaz, E. J. Sawyer, D.J. Lipomi, Wearable organic solar cells with high cyclic bending stability: materials selection criteria, Sol. Energy Mater. Sol. Cells 144 (2016) 438–444.
[6] Y. Jin, J. Feng, X.-L. Zhang, M. Xu, Y.-G. Bi, Q.-D. Chen, H.-Y. Wang, H.-B. Sun, Surface-plasmon enhanced absorption in organic solar cells by employing a periodically corrugated metallic electrode, Appl. Phys. Lett. 101 (2012) 163303.
[7] Y. Jin, J. Feng, M. Xu, X.L. Zhang, L. Wang, Q.D. Chen, H.Y. Wang, H.B. Sun, Matching photocurrents of sub-cells in double-junction organic solar cells via coupling between surface plasmon polaritons and microcavity modes, Adv. Opt. Mater. 1 (2013) 809–813.

[8] M. Xu, J. Feng, Y.-S. Liu, Y. Jin, H.-Y. Wang, H.-B. Sun, Effective and tunable light trapping in bulk heterojunction organic solar cells by employing Au-Ag alloy nanoparticles, Appl. Phys. Lett. 105 (2014) 153303.

[9] A. Kojima, K. Teshima, Y. Shirai, T. Miyasaka, Organometal halide perovskites as visible-light sensitizers for photovoltaic cells, J. Am. Chem. Soc. 131 (2009) 6050–6051.

[10] W.S. Yang, J.H. Noh, N.J. Jeon, Y.C. Kim, S. Ryu, J. Seo, S.I. Seok, High-performance photovoltaic perovskite layers fabricated through intramolecular exchange, Science 348 (2015) 1234–1237.

[11] H. Azimi, T. Ameri, H. Zhang, Y. Hou, C.O.R. Quiroz, J. Min, M. Hu, Z.G. Zhang, T. Przybilla, G.J. Matt, A. Universal, Interface layer based on an amine-functionalized fullerene derivative with dual functionality for efficient solution processed organic and perovskite solar cells, Adv. Energy Mater. 5 (2015) 1401692.

[12] H. Zhou, Q. Chen, G. Li, S. Luo, T.-b Song, H.-S. Duan, Z. Hong, J. You, Y. Liu, Y. Yang, Interface engineering of highly efficient perovskite solar cells, Science 345 (2014) 542–546.

[13] S.-M. Park, Y.-J. Noh, S.-H. Jin, S.-I. Na, Efficient planar heterojunction perovskite solar cells fabricated via roller-coating, Sol. Energy Mater. Sol. Cells 155 (2016) 14–19.

[14] M. Park, H.J. Kim, I. Jeong, J. Lee, H. Lee, H.J. Son, D.E. Kim, M.J. Ko, Mechanically recoverable and highly efficient perovskite solar cells: investigation of intrinsic flexibility of organic-inorganic perovskite, Adv. Energy Mater. 5 (2015) 1501406.

[15] P. Bhatt, K. Pandey, P. Yadav, B. Tripathi, M.K. Pandey, M. Kumar, Investigating the charge carrier transport within the hole-transport material free perovskite solar cell processed in ambient air, Sol. Energy Mater. Sol. Cells 140 (2015) 320–327.

[16] L. Huang, Z. Hu, J. Xu, K. Zhang, J. Zhang, Y. Zhu, Multi-step slow annealing perovskite films for high performance planar perovskite solar cells, Sol. Energy Mater. Sol. Cells 141 (2015) 377–382.

[17] D. Liu, T.L. Kelly, Perovskite solar cells with a planar heterojunction structure prepared using room-temperature solution processing techniques, Nat. Photonics 8 (2014) 133–138.

[18] V. Zardetto, T.M. Brown, A. Reale, A. Di Carlo, Substrates for flexible electronics: a practical investigation on the electrical, film flexibility, optical, temperature, and solvent resistance properties, J. Polym. Sci. Part B: Polym. Phys. 49 (2011) 638–648.

[19] F. Di Giacomo, V. Zardetto, A. D'Epifanio, S. Pescetelli, F. Matteocci, S. Razza, A. Di Carlo, S. Licoccia, W.M. Kessels, M. Creatore, Flexible perovskite photovoltaic modules and solar cells based on atomic layer deposited compact layers and UV-irradiated $TiO_2$ scaffolds on plastic substrates, Adv. Energy Mater. 5 (2015) 1401808.

[20] M. Dianetti, F. Di Giacomo, G. Polino, C. Ciceroni, A. Liscio, A. D'Epifanio, S. Licoccia, T. Brown, A. Di Carlo, F. Brunetti, TCO-free flexible organo metal trihalide perovskite planar-heterojunction solar cells, Sol. Energy Mater. Sol. Cells 140 (2015) 150–157.

[21] H. Sung, N. Ahn, M.S. Jang, J.K. Lee, H. Yoon, N.G. Park, M. Choi, Transparent conductive oxide-free graphene-based perovskite solar cells with over 17% efficiency, Adv. Energy Mater. 6 (2016) 1501873.

[22] A.R. bin Mohd Yusoff, D. Kim, F.K. Schneider, W.J. da Silva, J. Jang, Au-doped single layer graphene nanoribbons for a record-high efficiency ITO-free tandem polymer solar cell, Energy Environ. Sci. 8 (2015) 1523–1537.

[23] I. Jeon, T. Chiba, C. Delacou, Y. Guo, A. Kaskela, O. Reynaud, E.I. Kauppinen, S. Maruyama, Y. Matsuo, Single-walled carbon nanotube film as electrode in indium-free planar heterojunction perovskite solar cells: investigation of electron-blocking layers and dopants, Nano Lett. 15 (2015) 6665–6671.

[24] J. Han, S. Yuan, L. Liu, X. Qiu, H. Gong, X. Yang, C. Li, Y. Hao, B. Cao, Fully indium-free flexible Ag nanowires/ZnO:F composite transparent conductive electrodes with high haze, J. Mater. Chem. A 3 (2015) 5375–5384.

[25] A. Kim, H. Lee, H.C. Kwon, H.S. Jung, N.G. Park, S. Jeong, J. Moon, Fully solution-processed transparent electrodes based on silver nanowire composites for perovskite solar cells, Nanoscale 8 (2016) 6308–6316.

[26] M. Kaltenbrunner, G. Adam, E.D. Głowacki, M. Drack, R. Schwödiauer, L. Leonat, D.H. Apaydin, H. Groiss, M.C. Scharber, M.S. White, Flexible high power-per-weight perovskite solar cells with chromium oxide-metal contacts for improved stability in air, Nat. Mater. 14 (2015) 1032–1039.

[27] M. Valipour, Optimization of neural networks for precipitation analysis in a humid region to detect drought and wet year alarms, Meteorol. Appl. 23 (2016) 91–100.

[28] S. Yannopoulos, G. Lyberatos, N. Theodossiou, W. Li, M. Valipour, A. Tamburrino, A. Angelakis, Evolution of water lifting devices (pumps) over the centuries worldwide, Water 7 (2015) 5031–5060.

[29] M. Valipour, M.A.G. Sefidkouhi, S. Eslamian, Surface irrigation simulation models: a review, Int. J. Hydrol. Sci. Technol. 5 (2015) 51–70.

[30] M. Valipour, Sprinkle and trickle irrigation system design using tapered pipes for pressure loss adjusting, J. Agric. Sci. 4 (2012).

[31] M. Mahdizadeh Khasraghi, M.A. Gholami Sefidkouhi, M. Valipour, Simulation of open-and closed-end border irrigation systems using SIRMOD, Arch. Agron. Soil Sci. 61 (2015) 929–941.

[32] M. Valipour, Comparison of surface irrigation simulation models: full hydrodynamic, zero inertia, kinematic wave, J. Agric. Sci. 4 (2012) 68.

[33] C. Roldán-Carmona, O. Malinkiewicz, R. Betancur, G. Longo, C. Momblona, F. Jaramillo, L. Camacho, H.J. Bolink, High efficiency single-junction semitransparent perovskite solar cells, Energy Environ. Sci. 7 (2014) 2968–2973.

[34] G.E. Eperon, V.M. Burlakov, A. Goriely, H.J. Snaith, Neutral color semitransparent microstructured perovskite solar cells, ACS Nano 8 (2013) 591–598.

[35] Y. Guo, K. Shoyama, W. Sato, E. Nakamura, Polymer stabilization of lead (II) perovskite cubic nanocrystals for semitransparent solar cells, Adv. Energy Mater. 6 (2016) 1502317.

[36] N.J. Jeon, J.H. Noh, Y.C. Kim, W.S. Yang, S. Ryu, S.I. Seok, Solvent engineering for high-performance inorganic-organic hybrid perovskite solar cells, Nat. Mater. 13 (2014) 897–903.

[37] J.W. Jung, S.T. Williams, A.K.-Y. Jen, Low-temperature processed high-performance flexible perovskite solar cells via rationally optimized solvent washing treatments, RSC Adv. 4 (2014) 62971–62977.

[38] L.K. Ono, S. Wang, Y. Kato, S.R. Raga, Y. Qi, Fabrication of semi-transparent perovskite films with centimeter-scale superior uniformity by the hybrid deposition method, Energy Environ. Sci. 7 (2014) 3989–3993.

[39] P. You, Z. Liu, Q. Tai, S. Liu, F. Yan, Efficient semitransparent perovskite solar cells with graphene electrodes, Adv. Mater. 27 (2015) 3632–3638.

[40] M.M. Tavakoli, L. Gu, Y. Gao, C. Reckmeier, J. He, A.L. Rogach, Y. Yao, Z. Fan, Fabrication of efficient planar perovskite solar cells using a one-step chemical vapor deposition method, Sci. Rep. 5 (2015) 14083.

[41] H. Dong, Z. Wu, B. Xia, J. Xi, F. Yuan, S. Ning, L. Xiao, X. Hou, Modified deposition process of electron transport layer for efficient inverted planar perovskite solar cells, Chem. Commun. 51 (2015) 8986–8989.

[42] Y. Chen, T. Chen, L. Dai, Layer-by-layer growth of $CH_3NH_3PbI_{3-x}Cl_x$ for highly efficient planar heterojunction perovskite solar cells, Adv. Mater. 27 (2015) 1053–1059.

[43] Y. Li, W. Sun, W. Yan, S. Ye, H. Peng, Z. Liu, Z. Bian, C. Huang, High-performance planar solar cells based on $CH_3NH_3PbI_{3-x}Cl_x$ perovskites with determined chlorine mole fraction, Adv. Funct. Mater. 25 (2015) 4867–4873.

[44] L. Huang, Z. Hu, G. Yue, J. Liu, X. Cui, J. Zhang, Y. Zhu, $CH_3NH_3PbI_{(3-x)}Cl_{(x)}$ films with coverage approaching 100% and with highly oriented crystal domains for reproducible and efficient planar heterojunction perovskite solar cells, Phys. Chem. Chem. Phys. 17 (2015) 22015–22022.

[45] S.R. Raga, M.-C. Jung, M.V. Lee, M.R. Leyden, Y. Kato, Y. Qi, Influence of air annealing on high efficiency planar structure perovskite solar cells, Chem. Mater. 27 (2015) 1597–1603.

[46] S. Schubert, J. Meiss, L. Müller-Meskamp, K. Leo, Improvement of transparent metal top electrodes for organic solar cells by introducing a high surface energy seed layer, Adv. Energy Mater. 3 (2013) 438–443.

[47] E. Della Gaspera, Y. Peng, Q. Hou, L. Spiccia, U. Bach, J.J. Jasieniak, Y.-B. Cheng, Ultra-thin high efficiency semitransparent perovskite solar cells, Nano Energy 13 (2015) 249–257.

[48] Y. Long, Improving optical performance of inverted organic solar cells by microcavity effect, Appl. Phys. Lett. 95 (2009) 193301.

[49] J. Meiss, M. Riede, K. Leo, Towards efficient tin-doped indium oxide (ITO)-free inverted organic solar cells using metal cathodes, Appl. Phys. Lett. 94 (2009) 013303.

[50] J.B. You, Z. Hong, Y.M. Yang, Q. Chen, M. Cai, T.-B. Song, C.-C. Chen, S. Lu, Y. S. Liu, H. Zhou, Y. Yang, Low-temperature solution-processed perovskite solar cells with high efficiency and flexibility, ACS Nano 8 (2014) 1674–1680.

[51] J.H. Heo, M.H. Lee, H.J. Han, B.R. Patil, J.S. Yu, S.H. Im, Highly efficient low temperature solution processable planar type $CH_3NH_3PbI_3$ perovskite flexible solar cells, J. Mater. Chem. A 4 (2016) 1572–1578.

[52] B. Susrutha, L. Giribabu, S.P. Singh, Recent advances in flexible perovskite solar cells, Chem. Commun. 51 (2015) 14696–14707.